Supplementary Information

Manipulatable Cascade Pumping Single-Photon Upconversion

Qi Xiao,[1,2] Wen Xu,[1]* Xiumei Yin,[1] Na Zhou,[1] Xinyao Dong,[1] Ge Zhu,[1] Xixian Luo,[1] Yinglin Song,[2]* Bin Dong[1]*

[1] School of Physics and Materials Engineering, Dalian Minzu University, 18 Liaohe West Road, Dalian 116600, P. R. China.
[2] School of Physics, Harbin Institute of Technology, Harbin 150001, P. R. China.
* Corresponding authors: xuwen@dlnu.edu.cn (Wen Xu); ylsong@hit.edu.cn (Yinglin Song); dong@dlnu.edu.cn (Bin Dong)

I. Supplementary Methods

Supplementary Note 1 - Transition rate equation for improved emission of RE^{3+}

To understand qualitatively the photophysical mechanism in this enhanced UC luminescence process, a set of rate equations were established based on the UC process:

$$dN_1 / dt = \sigma_{01}\rho N_0 + R_{21}^{'} N_2 - R_1 N_1 \tag{1}$$

$$dN_2 / dt = \sigma_{12}\rho N_1 - R_{21}^{'} N_2 - R_2 N_2 \tag{2}$$

$$N_{RE} = N_0 + N_1 + N_2 \tag{3}$$

where N_0, N_1, and N_2 denote the population densities of energy levels for RE^{3+}, respectively. N_{RE} is the nominal ion density corresponding to the doping concentration. R_1, R_2, and R_3 are the radiative rates of energy levels for RE^{3+}, respectively. R'_{ij} is non-radiative rate from level i to level j. ρ is the laser photon number density. σ_{ij} denotes the absorption cross-section between level i and j of RE^{3+}. Taking into account that the excited state populations ($<10^{16}$ ions/cm^3) are a small fraction of all the RE^{3+} ($N_{RE}>10^{20}$ ions/cm^3), it can be assumed that $N_0 \approx N_{RE}$. At steady state ($dN_i/dt=0$), the rate equations can be simplified as:

$$\sigma_{01}\rho N_0 - R_1 N_1 = 0 \tag{5}$$

$$\sigma_{12}\rho N_1 - R_2 N_2 = 0 \tag{6}$$

The emission intensities of emitting level (I_{RE}) can be given according to the population densities of N_2:

$$I_{RE} = R_2 N_2 = \frac{N_0 \sigma_{01}\sigma_{02}\rho^2}{R_1} \tag{7}$$

The UC rate equation indicates that the excitation photon density, absorption cross-sections and lifetimes of the energy levels play a key role in the emission of the target excited states.

Supplementary Note 2 - Machine learning algorithms

In this study, a multi-step computational strategy incorporating a bubble sort algorithm was developed to achieve optimal screening of host materials, doped rare earth ions, and dual excitation wavelengths. The bubble sort algorithm iteratively traverses the dataset, continuously comparing and swapping adjacent elements until the entire sequence is properly ordered and

screened [1,2]. First, a dedicated database is constructed by inputting systematic data, covering the intrinsic properties of various rare earth ions, their intrinsic energy level differences, characteristic target intermediate energy levels, as well as key parameters of different host materials (luminescence lifetime and phonon energy). After setting the target emission wavelength, the required energy level differences are quantitatively calculated and matched through programmed mathematical operations. Subsequently, all energy level data in the database are screened to identify energy level combinations that satisfy the dual-wavelength cascade pumping mechanism. Since UC luminescence performance is primarily determined by the phonon energy of the host material and the excited-state lifetime of the rare earth ions, the bubble sort algorithm is further employed to sort and optimally select the candidate host materials based on these two core parameters. Finally, by simply inputting the target emission requirement, the computational process outputs the optimal matching scheme, including the suitable rare earth ion species, host material system, characteristic intermediate energy levels, and optimal excitation laser wavelengths, thereby ensuring efficient UC luminescence.

In the numerical screening stage, the algorithm employs a nearest-neighbor search strategy based on linear traversal and threshold constraints. During execution, the algorithm performs a complete sequential traversal of the target numerical column, calculating the absolute deviation between each value and the preset target value. Among all candidate values whose deviations do not exceed the set threshold, the value with the smallest deviation from the target is selected as the final nearest neighbor, serving as the reference point for subsequent combinatorial calculations and indicator solving. This search strategy offers three significant advantages. First, it is simple to implement and highly stable, requiring no complex data preprocessing and being directly applicable to ordered or unordered small-scale numerical sequences. Second, the matching accuracy is controllable; the threshold parameter flexibly defines the valid matching range, preventing outliers and invalid values from interfering with the results. Third, the computational efficiency is high, as the algorithm completes the search with only a single linear traversal, resulting in low time complexity and good execution performance and practicality in engineering applications. In addition, the algorithm incorporates a well-designed two-level fault tolerance mechanism to ensure the robustness of the overall workflow and the regularity of the output results. When no nearest neighbor satisfying the threshold condition exists in the numerical

sequence, the algorithm immediately terminates the subsequent combinatorial calculation process for the current material and returns an empty result set, thereby avoiding invalid computations and error propagation.

Supplementary Note 3 - Materials and Synthesis route

Raw materials of $NaYF_4$ phosphors: Lanthanide oxides (Y_2O_3, Ho_2O_3; 99.99%), NH_4HF_2 and Na_2SiF_6 were used as the primary materials.

Synthesis of $NaYF_4$ phosphors: The $NaYF_4$:1%Ho^{3+} phosphors were synthesized by the solid state reaction. All primary materials can be used without further purification. First, the reactants were weighed according to the stoichiometric ratio, and then ground them for 30 minutes in a mortar to mix the reactants thoroughly. The reactants were first sintered at 200 °C for 2 hours and then calcined at 650 °C for 4 hours. The entire process needs to be carried out in the Ar atmosphere. Finally, the prepared samples were fully ground after cooling for testing.

Raw materials of Y_2O_3 phosphors: Lanthanide oxides (Y_2O_3, Ho_2O_3; 99.99%) were used as the primary materials.

Synthesis of Y_2O_3 phosphors: The Y_2O_3:1%Ho^{3+} phosphors were synthesized by the solid state reaction. All primary materials can be used without further purification. First, the reactants were weighed according to the stoichiometric ratio, and then ground them for 30 minutes in a mortar to mix the reactants thoroughly. The reactants were calcined at 1250 °C in the air for 4 hours. Finally, the prepared samples were fully ground after cooling for testing.

Raw materials of $La_2Mo_2O_9$ phosphors: Lanthanide oxides (La_2O_3, Ho_2O_3; 99.99%) and MoO_3 (99.5%) were used as the primary materials.

Synthesis of $La_2Mo_2O_9$ phosphors: The $La_2Mo_2O_9$:1%Ho^{3+} phosphors were synthesized by the solid state reaction. All primary materials can be used without further purification. First, the reactants were weighed according to the stoichiometric ratio, and then ground them for 30 minutes in a mortar to mix the reactants thoroughly. The reactants were calcined in the air at 1000 °C for 10 hours. Finally, the prepared samples were fully ground after cooling to room temperature naturally for testing.

Structure and morphology characterization: X-ray diffraction (XRD) was performed by using the Shimadzu-6000 X-ray diffractometer with Cu Kα radiation (λ=0.15406 nm, 40 kV, 40 mA,

2θ=10-70°). Scanning electron microscopic (SEM) images were acquired with a Hitachi S-4800 scanning electron microscope. Transmission electron microscopic (TEM) and high resolution transmission electron microscopic (HRTEM) images of samples were measured by using a JEM-2100F transmission electron microscope.

Optical properties measurement: UC luminescence spectra and decay curves were measured by a Jobin Yvon iHR550 monochromator equipped with R928 and H10220B-75 photomultiplier tubes from Hamamatsu Photonics and a Tektronix DPO 5104 digital oscilloscope using 808 nm, 980 nm, 1208 nm, 1532 nm and 2096 nm laser diodes (maximum power of 1.0 W for the 1532 nm laser, maximum power of 2.0 W for 808 nm, 980 nm, and 2096 nm laser, maximum power of 3.0 W for the 1208 nm laser), and a pulsed work Horizon OPO laser, for signal collection from 400 nm to 1700 nm. In addition, a tunable Nd:YAG laser pumped OPO laser was used as the excitation source (e.g., 760 nm), with a pulse duration of 20 ns, repetition frequency of 5 Hz and a line width of 4-7 cm^{-1}. The UC luminescence images were captured using a Canon EOS 5D Mark III digital camera (Tv=1:1250, Lens: EF 24-70 mm f/2.8L II USM, Av=2.8, ISO=12800). The 2004 nm detector chip, supplied by INP Photonics (Suzhou) Co., Ltd., is a photodiode designed for carbon dioxide sensing applications, model number INP-PCS-2004N-A09-01. It operates within a wavelength range of 900-2200 nm and a temperature range of -40 to 80 °C.

Supplementary Note 4 - Energy transfer efficiency of $NaYS_2$ co-doped with Ho^{3+}-Yb^{3+} and Ho^{3+}-Tm^{3+}

Fig. 4 displays decay curves of $^5I_6$ level (Ho^{3+}) with various concentrations of Tm^{3+} under dual-wavelength (808 nm and 1208 nm) cascade pumping. The decay time constants of $^5I_6$ level for Ho^{3+} drop from 1523 μs to 146 μs as the concentration of Tm^{3+} increases from 0 mol% to 2 mol%. This is mainly attributed to the energy transfer from Ho^{3+} to Tm^{3+} by $^5I_6(Ho^{3+})\rightarrow{}^3H_5(Tm^{3+})$. The energy transfer efficiency (η) can be described by the following equation [3,4]:

$$\eta = 1 - \frac{\tau_d}{\tau_{d0}} \tag{1}$$

where τ_d and τ_{d0} are the lifetimes of the corresponding excited states for donor in the presence and absence of the acceptor. The calculated energy transfer efficiencies of Ho^{3+}:$^5I_6\rightarrow Tm^{3+}$:$^3H_5$ reaches

78.6% in $NaYS_2$:5mol%Ho^{3+}, 0.5mol%Tm^{3+}. These results show that appropriate introduction of other RE^{3+} under dual-wavelength cascade pumping can directionally change the energy transfer path, thereby achieving the emission of specific energy levels.

II. Supplementary Figures

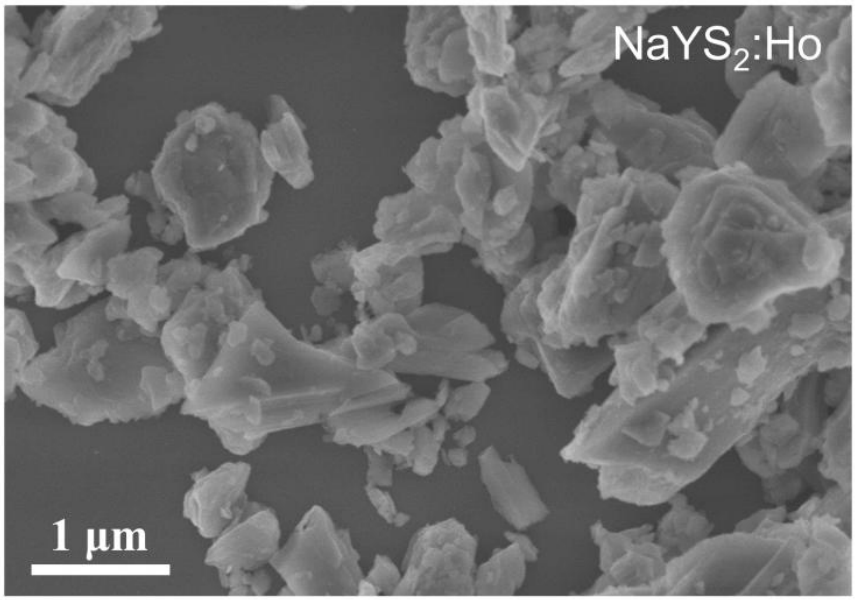

Supplementary Figure 1. SEM morphology characterization of $NaYS_2$. SEM image of Ho^{3+} single-doped $NaYS_2$ crystals. The synthesized sample presents highly aggregated crystallite state with a size of micron.

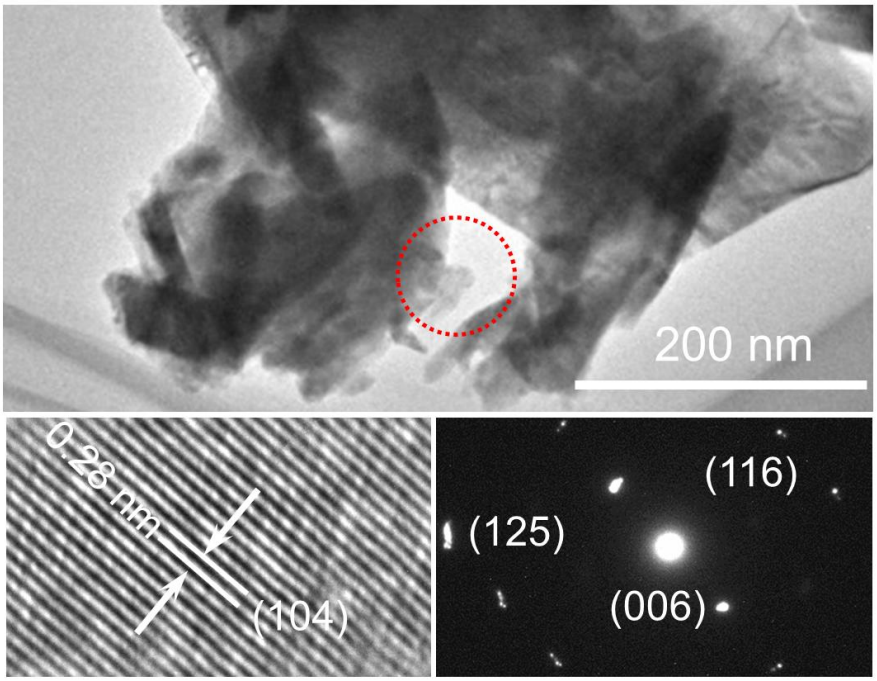

Supplementary Figure 2. TEM morphology characterization of $NaYS_2$. TEM image, high-resolution TEM image (bottom left) and Fourier-transform diffraction pattern (bottom right) of $NaYS_2$:Ho^{3+}.

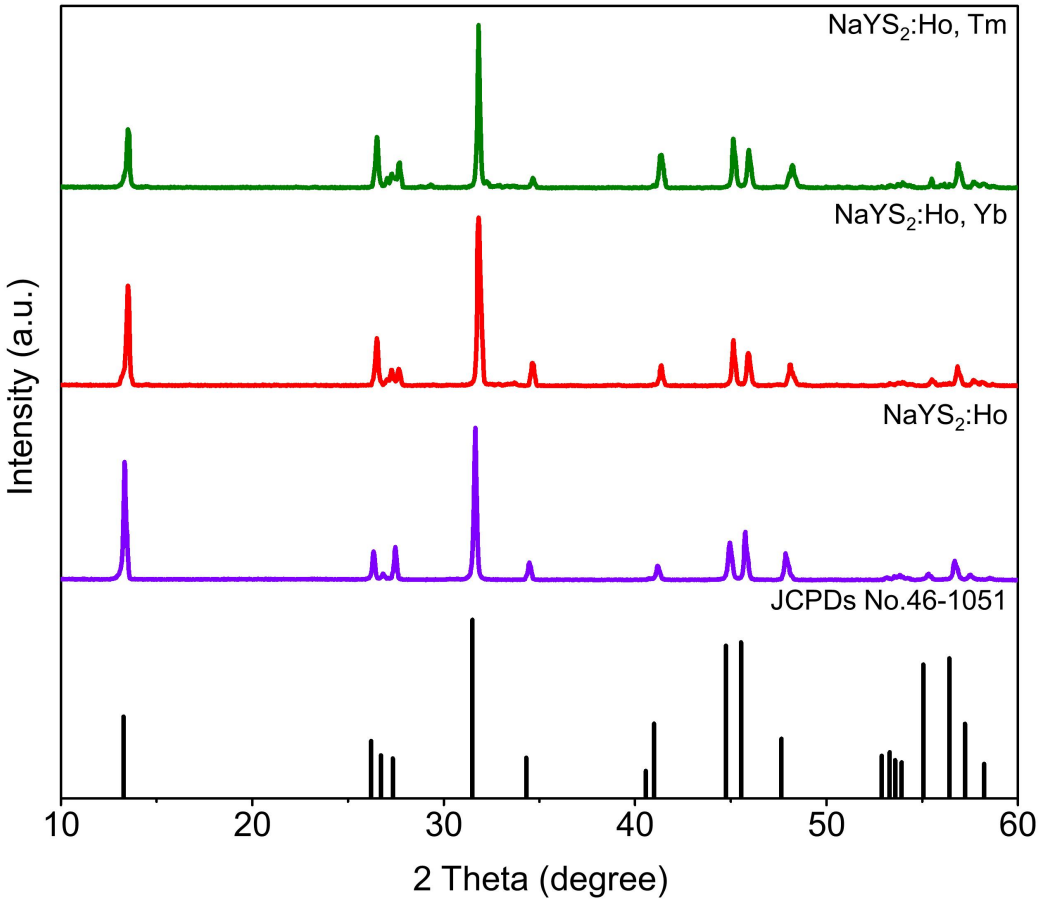

Supplementary Figure 3. Phase structure characterization of $NaYS_2$. XRD patterns of Ho^{3+} single-doped $NaYS_2$ and Ho^{3+}-Ln^{3+} (Ln^{3+}=Tm^{3+}, Yb^{3+}) co-doped $NaYS_2$ phosphors prepared at 800 °C.

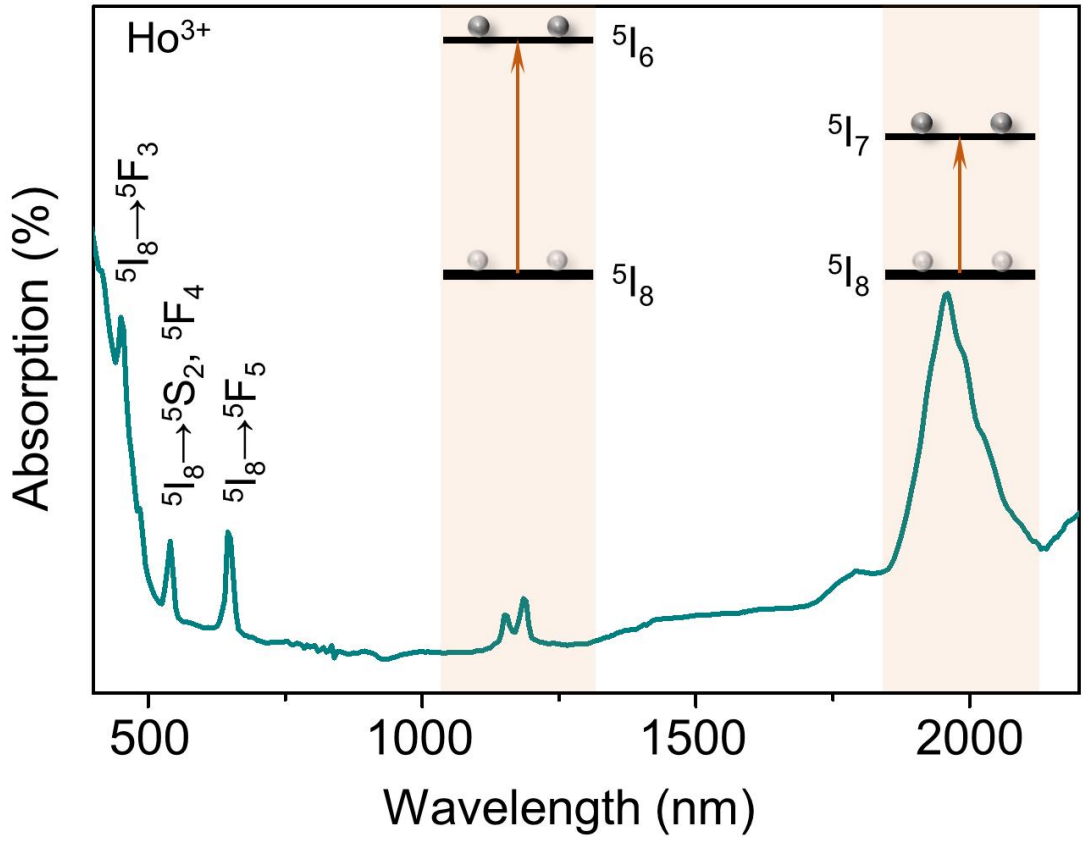

Supplementary Figure 4. Absorption spectrum of Ho^{3+}. It is possible to realize the re-absorption process of Ho^{3+} when the intermediate excited state ($^5I_7$ or $^5I_6$) is populated by a large number of electrons to form a new "ground state".

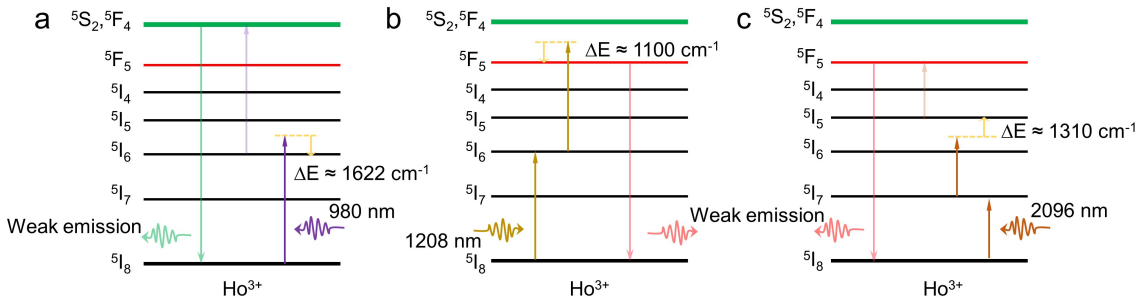

Supplementary Figure 5. Schematic diagram of the energy-level population of Ho^{3+} under single-wavelength excitation. Proposed mechanism of UC luminescence for $NaYS_2$:Ho^{3+} under (a) 980 nm, (b) 1208 nm and (c) 2096 nm excitation. Under 980 nm, 1208 nm and 2096 nm excitation, the electrons are populated on emitting level of Ho^{3+} through continuous absorption of single-wavelength photons. However, the serious mismatch between energy level gap and excitation energy makes it difficult to achieve effective population of emitting level of Ho^{3+} (The difference of energy level and excited wavelength: ΔE=~1622 cm^{-1} for 980 nm excitation, ΔE=~1100 cm^{-1} for 1208 nm excitation, and ΔE=~1310 cm^{-1} for 2096 nm excitation), resulting in weak UC emission under single-wavelength excitation.

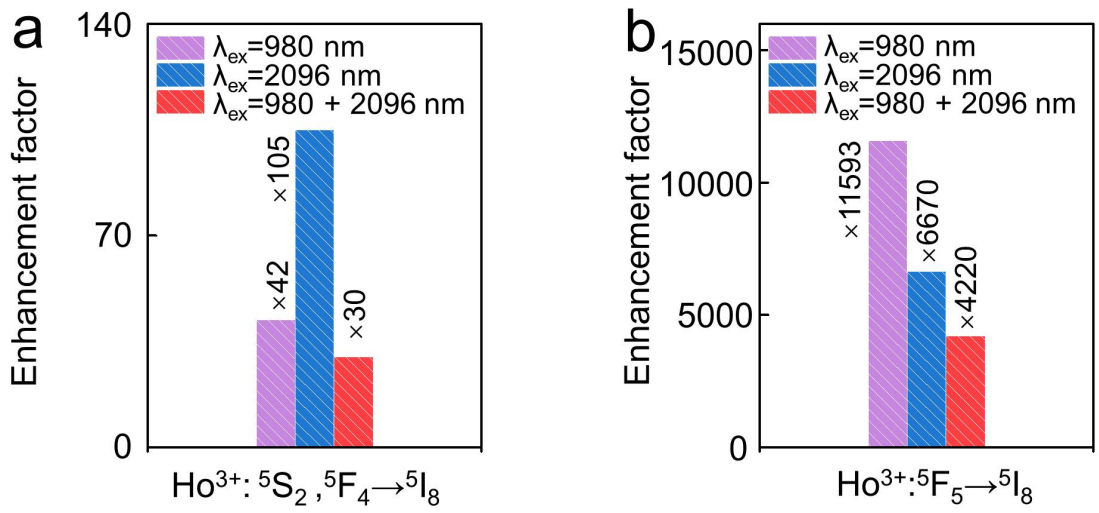

Supplementary Figure 6. Emission enhancement of $NaYS_2$:1mol%Ho^{3+} under cascade pumping. Histogram of emission enhancement factors for Ho^{3+} single-doped $NaYS_2$ under dual-wavelength cascade pumping, for transitions (a) $^5S_2$,$^5F_4$→$^5I_8$ and (b) $^5F_5$→$^5I_8$. Under cascade excitation at 980 nm and 2096 nm, the green emission intensity (Ho^{3+}: $^5S_2$,$^5F_4$→$^5I_8$) is 42 times that under 980 nm alone, 105 times that under 2096 nm alone, and 30 times the sum of the two single excitations. For the red emission (Ho^{3+}: $^5F_5$→$^5I_8$), the cascade excitation yields intensities enhancements of 11593, 6670, and 4220 times corresponding to the respective single excitations and their sum.

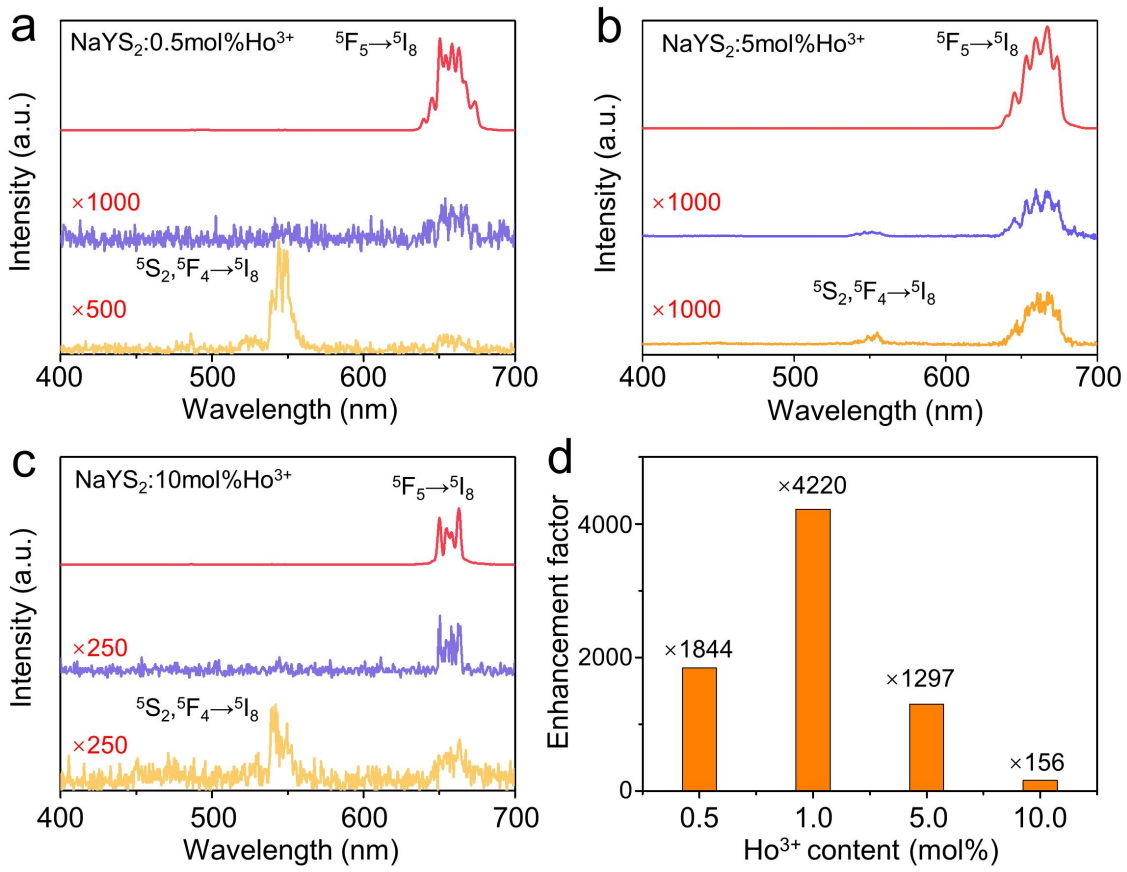

Supplementary Figure 7. Emission enhancement of Ho^{3+} with various concentrations under cascade pumping. (a-c) The UC emission spectra of $NaYS_2$:xHo^{3+} (x=0.5, 5.0, 10.0 mol%) under single/dual-wavelength excitation. (d) Histogram of enhancement factor with various Ho^{3+} concentration under dual-wavelength excitation.

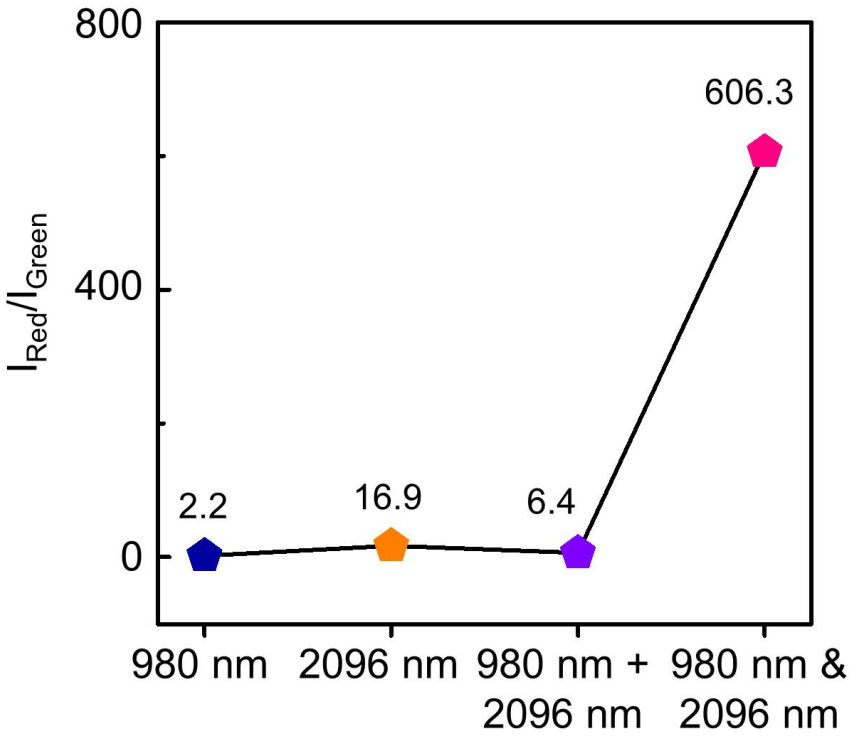

Supplementary Figure 8. I_R/I_G (Red and green emission intensity ratio) variation with various excitation modes. I_R/I_G of $NaYS_2:Ho^{3+}$ under 980 nm, 2096 nm, 980 nm + 2096 nm and dual-wavelength (980 nm & 2096 nm) cascade pumping. Compared with the I_R/I_G values of single-wavelength excitation or two wavelengths superimposed emission, the dual-wavelength cascade pumping can effectively achieve the red emission of $NaYS_2:Ho^{3+}$, thereby resulting in a considerable improvement in I_R/I_G values.

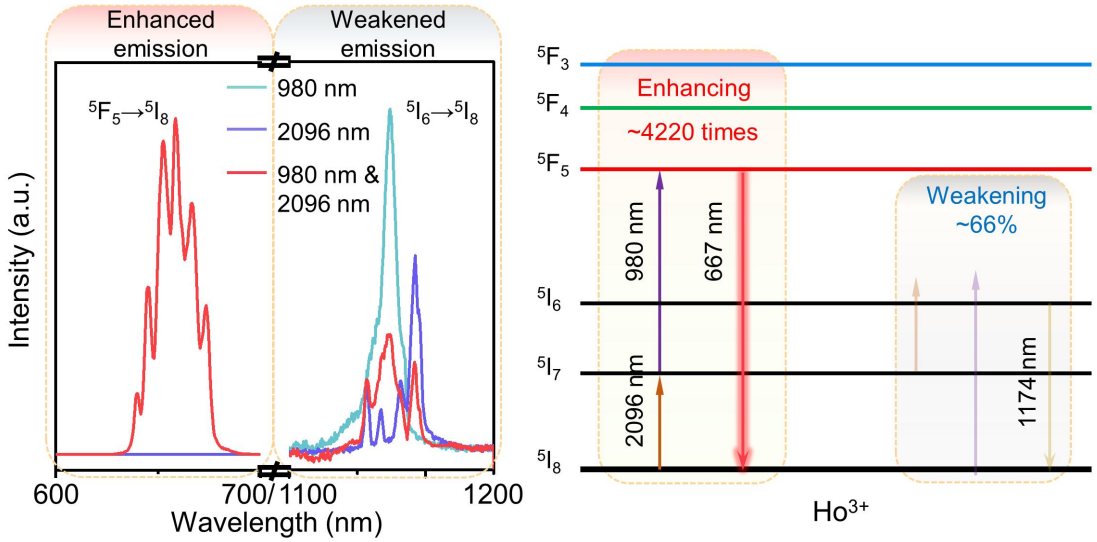

Supplementary Figure 9. Comparison of red and NIR emission intensity variations in $NaYS_2:Ho^{3+}$ under cascade excitation. The emission contrast spectra of $^5F_5 \rightarrow {}^5I_8$ and $^5I_6 \rightarrow {}^5I_8$ for $NaYS_2:Ho^{3+}$ (1 mol%) under single/dual-wavelength excitation, accompanied with a simple transition mechanism. Contrary to the enhancement of visible emission, NIR emission of $^5I_6 \rightarrow {}^5I_8$ exhibits a obvious decrease under dual-wavelength cascade pumping.

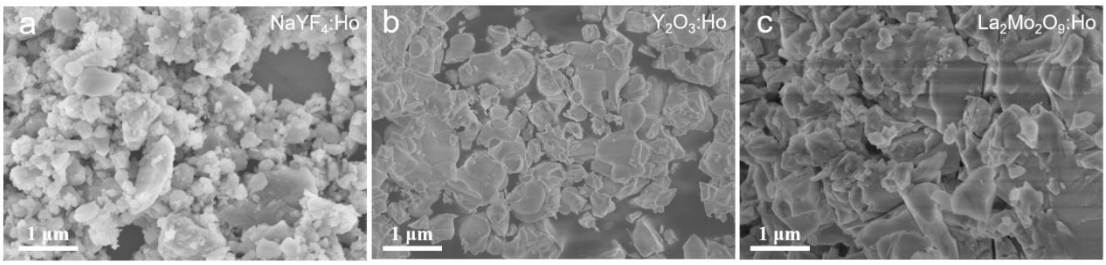

Supplementary Figure 10. SEM morphology characterization of $NaYF_4/Y_2O_3/La_2Mo_2O_9$. SEM images of Ho^{3+} single-doped (a) $NaYF_4$, (b) Y_2O_3, and (c) $La_2Mo_2O_9$ crystals. The synthesized samples present highly aggregated crystallite states with a size of micron.

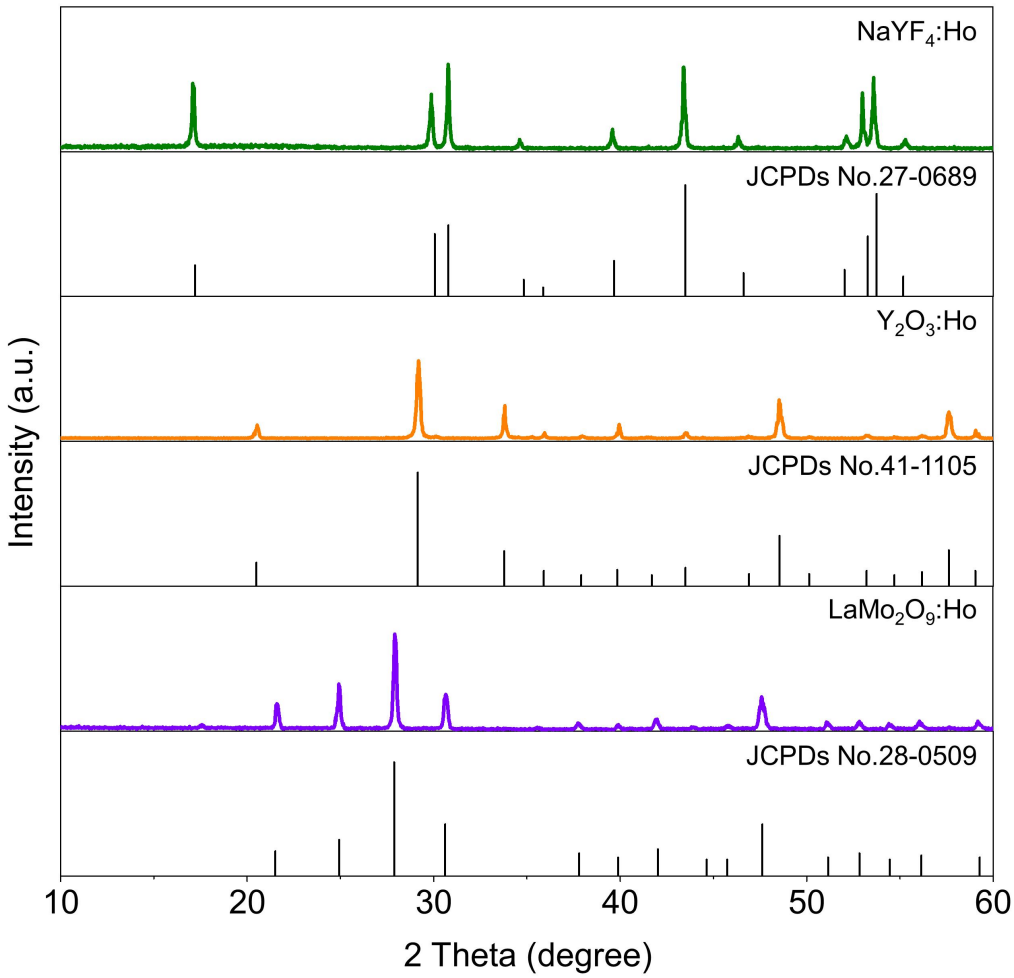

Supplementary Figure 11. Phase structure characterization of $NaYF_4/Y_2O_3/La_2Mo_2O_9$. XRD patterns of Ho^{3+} single-doped $NaYF_4/Y_2O_3/La_2Mo_2O_9$ phosphors. All the prepared samples are pure phase.

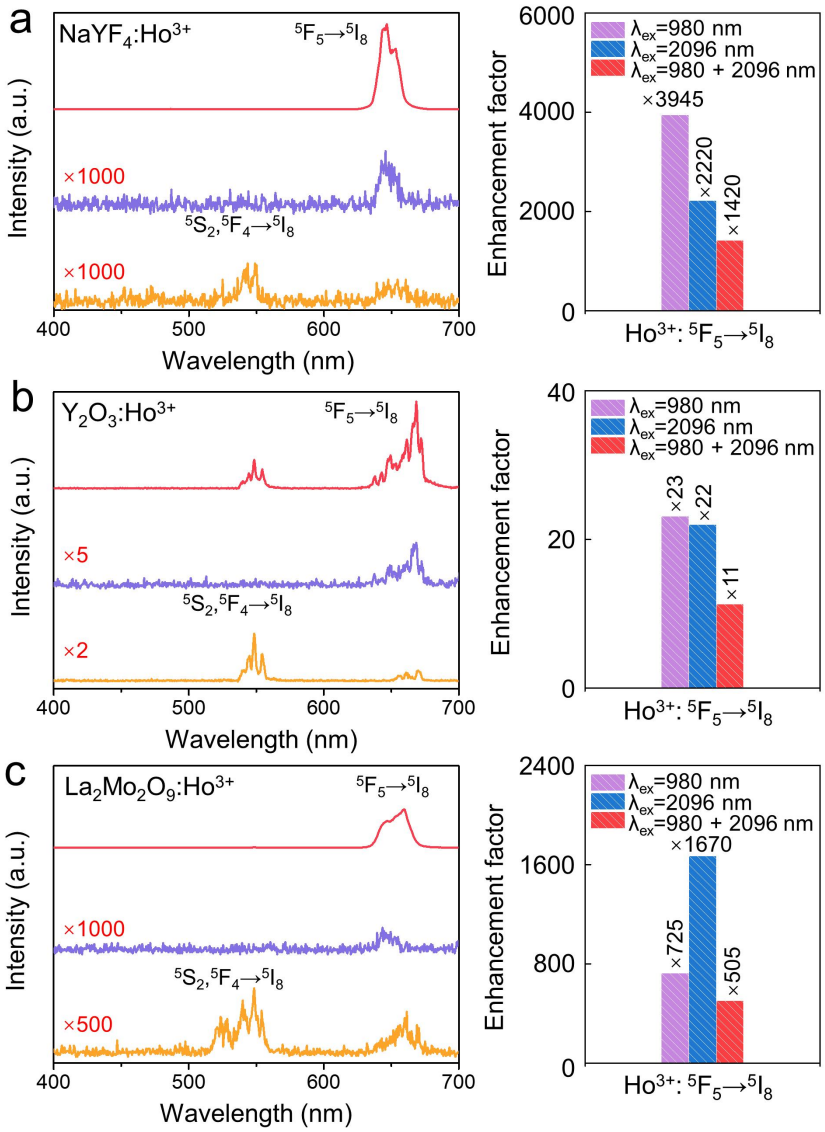

Supplementary Figure 12. Emission enhancement of $NaYF_4/Y_2O_3/La_2Mo_2O_9$:1mol%$Ho^{3+}$ under cascade pumping. The UC emission spectra of (a) $NaYF_4$:1mol%Ho^{3+}, (b) Y_2O_3:1mol%Ho^{3+} and (c) $La_2Mo_2O_9$:1mol%Ho^{3+} under single/dual-wavelength excitation, accompanied by histograms of enhancement multiples compared to different wavelengths (980 nm, 2096 nm and 980 nm + 2096 nm). For the Ho^{3+} $^5F_5 \rightarrow {}^5I_8$ transition (red emission) under cascade excitation of 980 nm & 2096 nm, the red emission intensity is 3945 ($NaYF_4$), 23 (Y_2O_3), 725 ($La_2Mo_2O_9$) times that under 980 nm single excitation, 2220 ($NaYF_4$), 22 (Y_2O_3), 1670 ($La_2Mo_2O_9$) times that under 2096 nm single excitation, and 1420 ($NaYF_4$), 11 (Y_2O_3), 505 ($La_2Mo_2O_9$) times the sum of the two single excitation intensities.

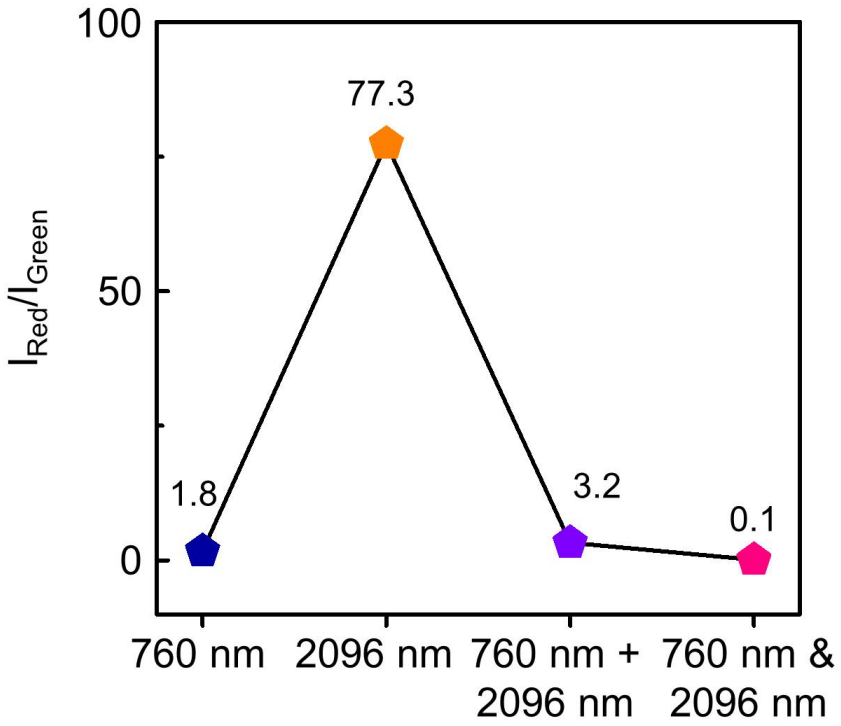

Supplementary Figure 13. I_R/I_G variation with various excitation modes. I_R/I_G of $NaYS_2:Ho^{3+}$ under 760 nm, 2096 nm and dual-wavelength (760 nm & 2096 nm) cascade pumping.

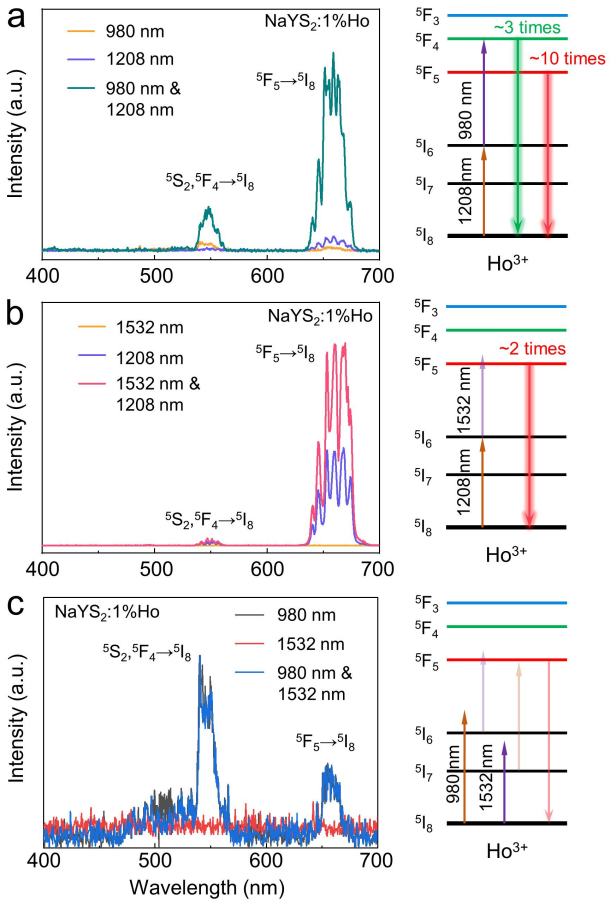

Supplementary Figure 14. UC luminescence and population mechanisms of $NaYS_2:Ho^{3+}$ under cascaded pumping with different wavelength combinations. The UC emission spectra of $NaYS_2:Ho^{3+}$ (1 mol%) under various single/dual-wavelength excitation ((a) 980 nm and 1208 nm; (b) 1208 nm and 1532 nm; (c) 980 nm and 1532 nm), accompanied with a simple transition mechanism of single-photon UC by LEGO-inspired photon stacking.

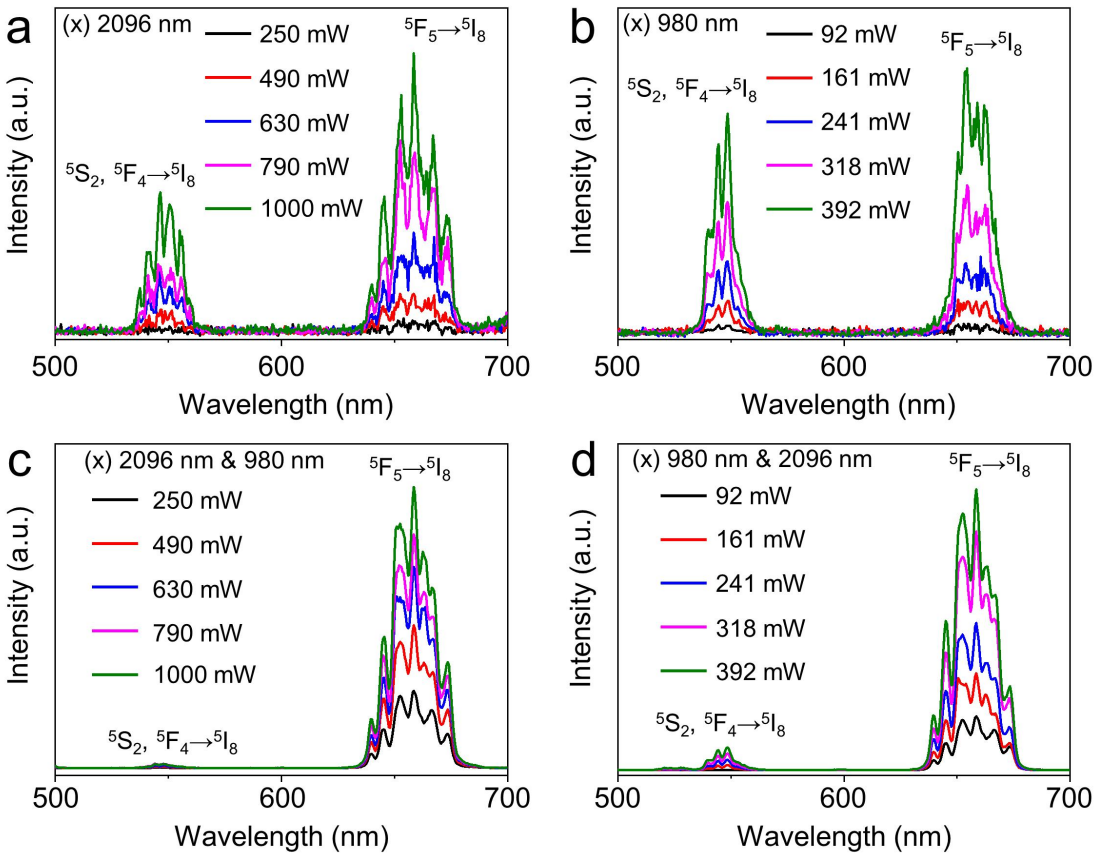

Supplementary Figure 15. Power-dependent spectra under single-wavelength excitation and cascade pumping. (a, b) UC emission spectra of $NaYS_2:Ho^{3+}$ under single-wavelength (2096 nm and 980 nm) excitation. (c, d) UC emission spectra of $NaYS_2:Ho^{3+}$ obtained by adjusting the pumping power of single-wavelength excitation source under dual-wavelength cascade pumping (a:(250-1000 mW) 2096 nm & 92 mW 980 nm; b: (92-392 mW) 980 nm & 250 mW 2096 nm).

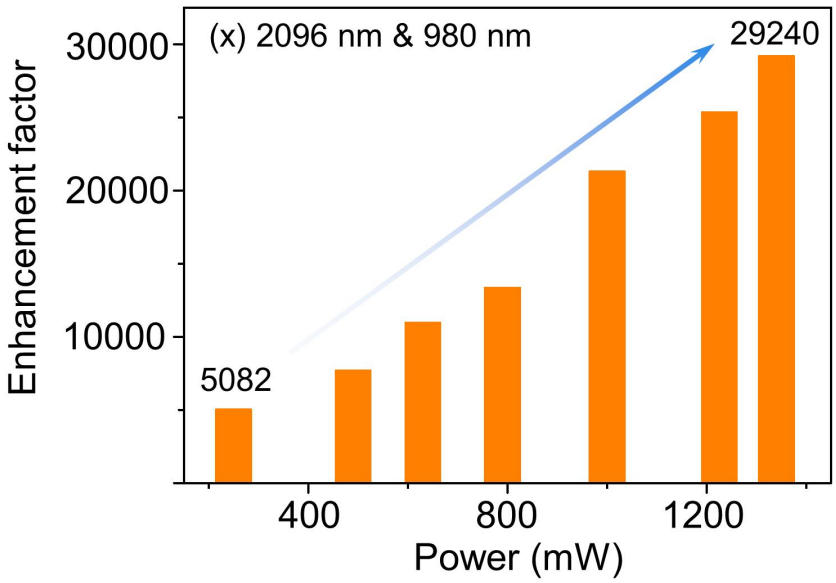

Supplementary Figure 16. Power-dependent enhancement factor of cascade pumping relative to 980 nm excitation. The enhancement factor of typical red and green UC emission intensities from Ho^{3+} under dual-wavelength of (x)2096 & 980 nm excitation compared to under single-wavelength of 980 nm excitation. As the 2096 nm laser power increases from 250 mW to 1340 W with fixed 980 nm laser power of 92 mW, the red emission intensity are gradually enhanced from 5082 times to 29240 times compared with the single-wavelength of 980 nm excitation case.

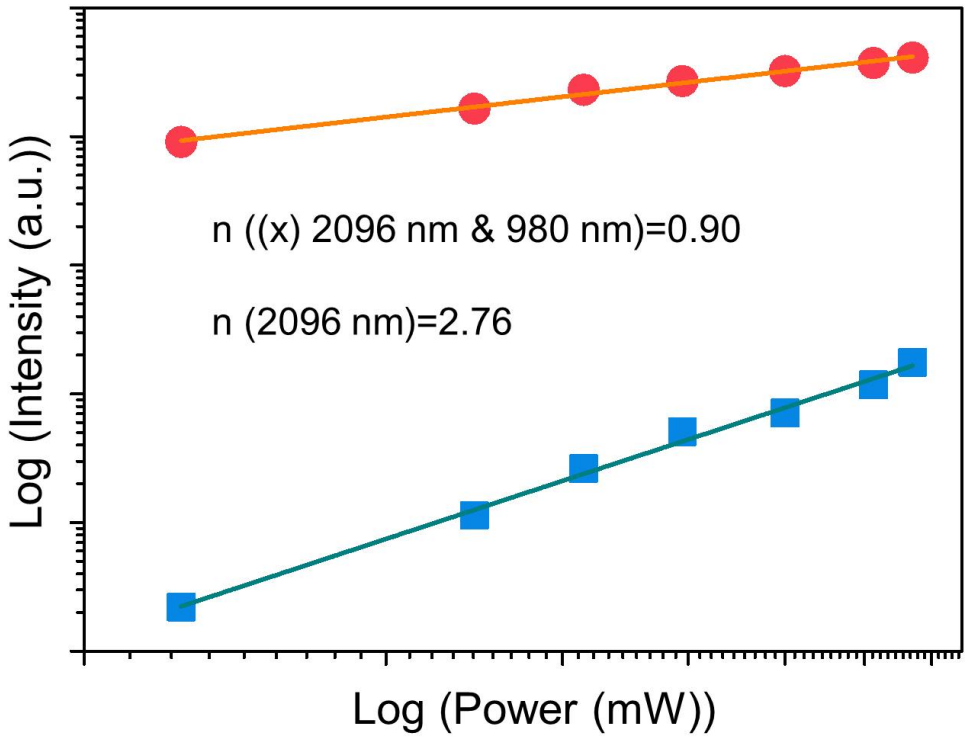

Supplementary Figure 17. Power dependent UC emissions under cascade pumping and 2096 nm excitation. Double logarithmic dependence of red emission intensity on the laser powers of single-wavelength of 2096 nm excitation or dual-wavelength cascade pumping with the fixed power of 980 nm excitation.

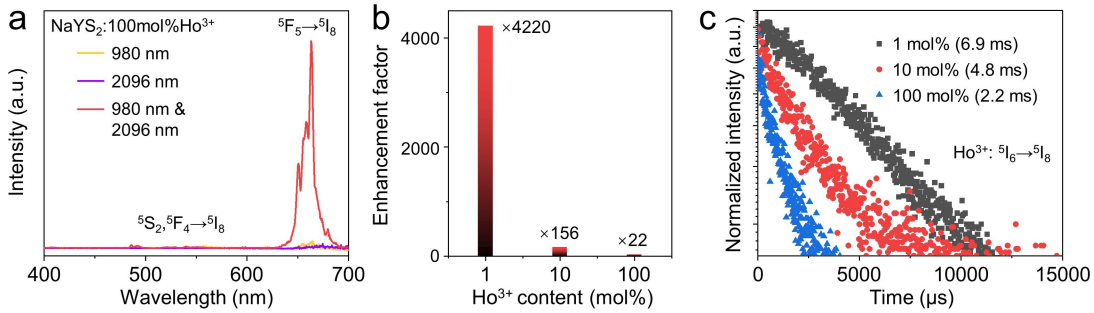

Supplementary Figure 18. Comparison and mechanistic analysis of emission enhancement of Ho^{3+} at different concentrations. (a) The UC emission spectra of $NaHoS_2$ under single/dual-wavelength excitation. (b) Histogram of enhancement factor with various Ho^{3+} concentration (1, 10, 100 mol%) under dual-wavelength excitation. (c) The normalized decay curves of $^5I_6$ (Ho^{3+}) energy levels with various components of Ho^{3+}. The intermediate-state lifetime exhibits a positive correlation with the enhancement of cascade-pumping UC luminescence, i.e., a longer excited-state lifetime is more favorable for effectively serving as a virtual ground state to facilitate re-excitation, thereby enabling efficient cascade pumping UC.

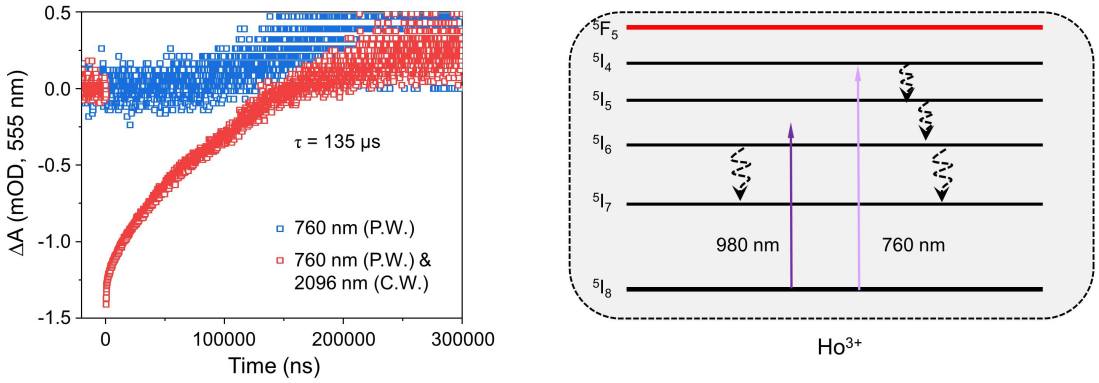

Supplementary Figure 19. Transient absorption and population mechanisms of the green-emitting levels in Ho^{3+}. Ultrafast transient absorption kinetic curves of Ho^{3+} with a probe wavelength of 555 nm and the rapid non-radiative relaxation process of electrons inside Ho^{3+} under single-wavelength excitation of 980 nm or 760 nm.

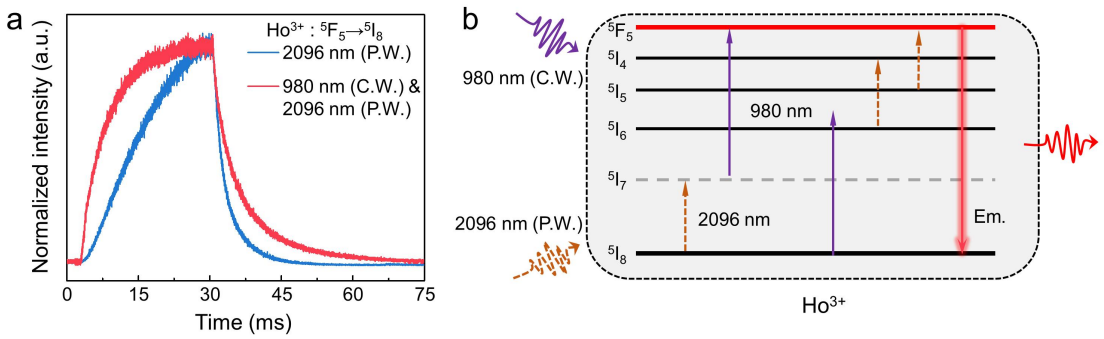

Supplementary Figure 20. UC luminescence dynamics in $NaYS_2:Ho^{3+}$. (a) Time-dependent red (667 nm) emission profiles of $NaYS_2:Ho^{3+}$ under pulsed dual-wavelength excitation with a duration time (pulse width) of 30 ms. 2096 nm laser as P.W. beam; 980 nm laser as C.W. beam. (b) Mechanism model of energy levels for modulation of red UC luminescence upon cascade pumping mode.

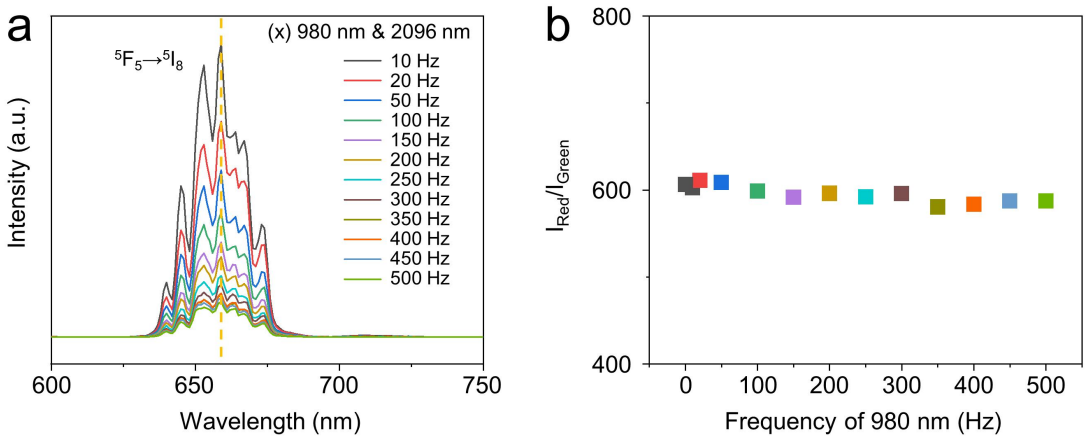

Supplementary Figure 21. Frequency-dependent luminescence properties of $NaYS_2:Ho^{3+}$. (a) The UC emission spectra and (b) I_{Red}/I_{Green} of $NaYS_2:Ho^{3+}$ (1 mol%) under dual-wavelength cascade pumping of 980 nm and 2096 nm with different excitation frequencies.

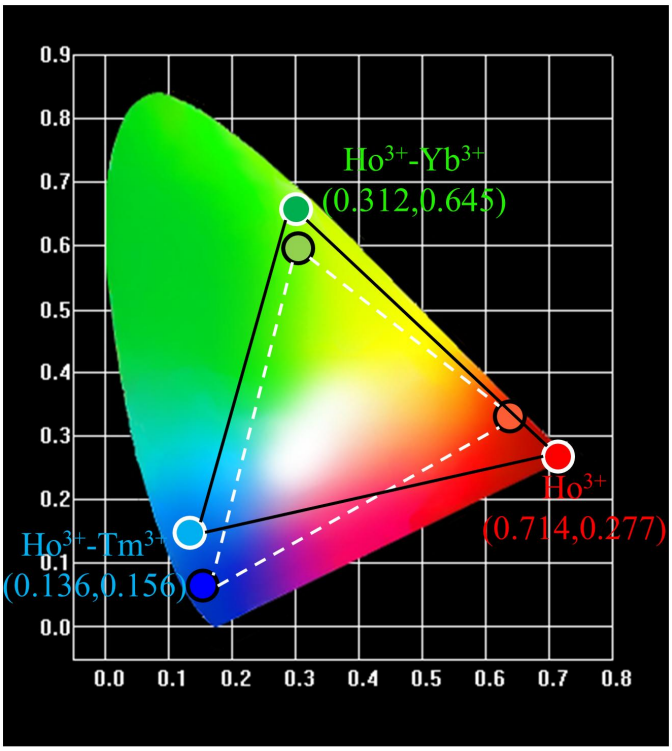

Supplementary Figure 22. UC luminescence color. CIE color coordinates of the Ho^{3+}, Ho^{3+}-Yb^{3+}, and Ho^{3+}-Tm^{3+} codoped $NaYS_2$ systems. The black solid triangle represents the color gamut of the samples, while the white dashed triangle indicates the standard sRGB color gamut.

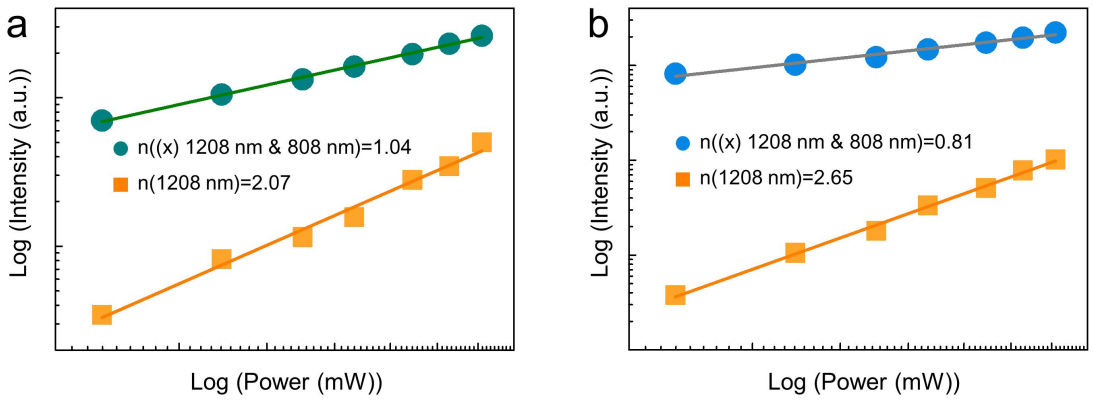

Supplementary Figure 23. Power dependent UC emissions of $NaYS_2:Ho^{3+},Yb^{3+}$ and $NaYS_2:Ho^{3+},Tm^{3+}$. Double logarithmic dependence of emission intensity on the laser powers of single-wavelength of 1208 nm excitation or dual-wavelength cascade pumping with the fixed power of 808 nm excitation in (a) $NaYS_2:Ho^{3+},Yb^{3+}$ and (b) $NaYS_2:Ho^{3+},Tm^{3+}$.

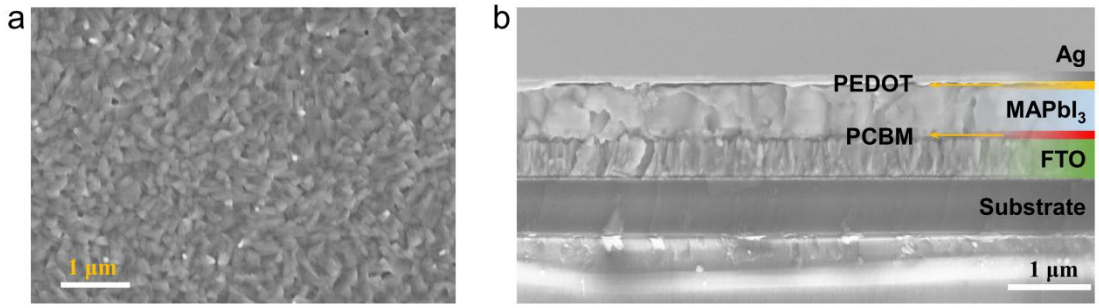

Supplementary Figure 24. SEM characterization of the fabricated PDs. (a) Top view SEM image of the perovskite structured $MAPbI_3$ hybrid film. (b) Side view SEM image of PDs. The PDs structure, from bottom to top, consists of a glass substrate, a FTO transparent conductive electrode, PCBM electron transport layer, a $MAPbI_3$ perovskite absorber layer, PEDOT hole transport layer, and Ag top electrode. The yellow arrows indicate the positions of the PCBM and PEDOT layers, respectively. The scale bar corresponds to 1 μm, providing a reference for estimating the thickness of each layer. The $MAPbI_3$ perovskite layer exhibits dense and continuous grains, with clear and uniform interfaces between adjacent layers, confirming the high-quality film deposition and good interlayer contact in the fabricated device.

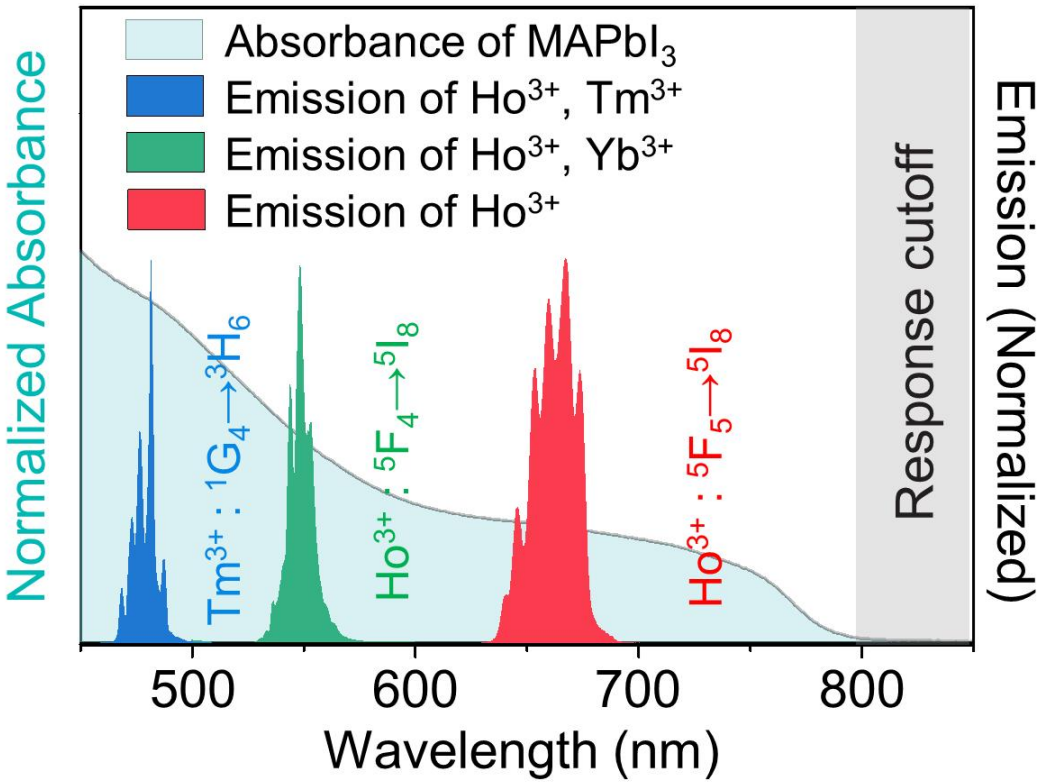

Supplementary Figure 25. Absorption of $MAPbI_3$ films and UC emission of three primary colors (R: $^5F_5 \rightarrow {}^5I_8$, G: $^5S_2, {}^5F_4 \rightarrow {}^5I_8$, and B: $^1G_4 \rightarrow {}^3H_6$). The $MAPbI_3$ films show the strong absorption of visible light and almost no response of NIR light exceeding 800 nm.

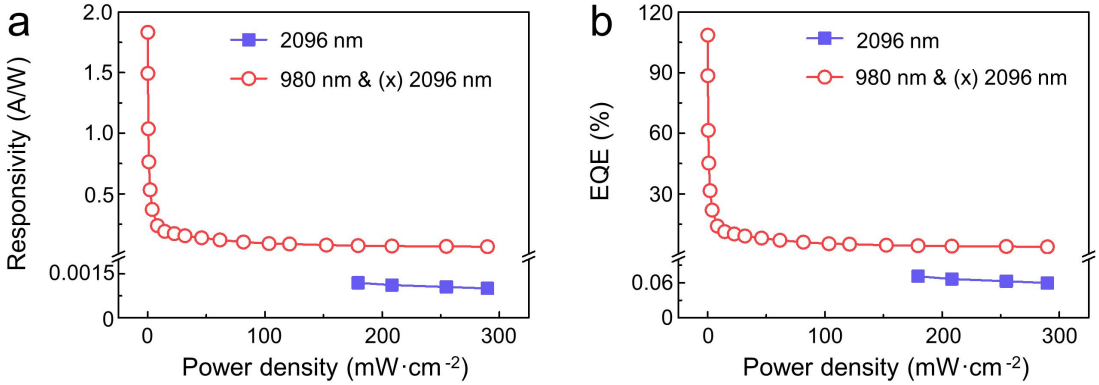

Supplementary Figure 26. The responsivity (*R*) and (b) external quantum efficiency (*EQE*) parameters of $NaYS_2:Ho^{3+}$-based PDs. Power density dependence of (a) *R* and (b) *EQE* for 2096 nm NIR light detection with or without 980 nm light assistance. $R=(I_{light}-I_{dark})/PS$ and $EQE=Rhc/\lambda e$. Where I_{light} and I_{dark} are photocurrents under light and dark environments, *P* is intensity of the irradiated light, *S* is the effective irradiated area. *h*, *c*, and *e* are both constant, representing Planck's constant, light velocity, and elementary charge. Notably, the UC-based PDs is specifically designed for the detection of the 2096 nm signal. The 980 nm laser serves merely as an auxiliary reference light source and is not part of the signal to be detected. Therefore, when evaluating the detection performance for 2096 nm, the 980 nm pump should not be considered.

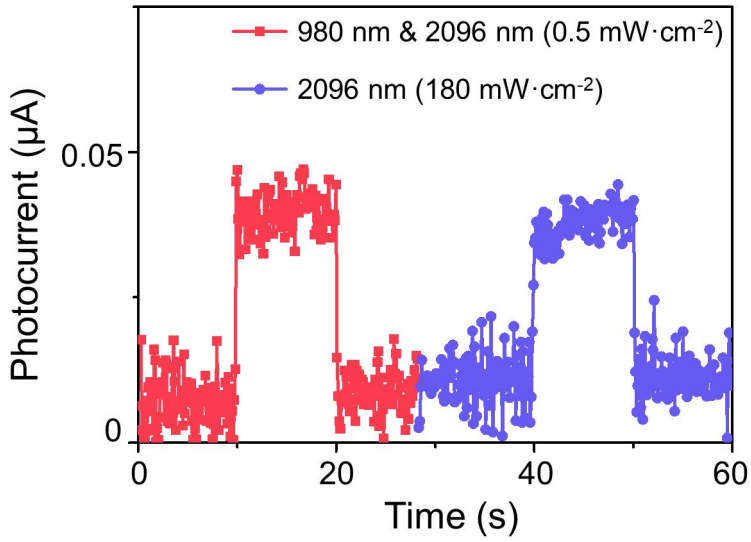

Supplementary Figure 27. Detection threshold of $NaYS_2:Ho^{3+}$-based PDs. On-off switching currents of the photodetectors under single-excitation of 2096 nm (power densities: 180 mW/cm^2) and dual-excitation of 980 nm (power densities: 20 mW/cm^2) and 2096 nm (power densities: 0.5 mW/cm^2).

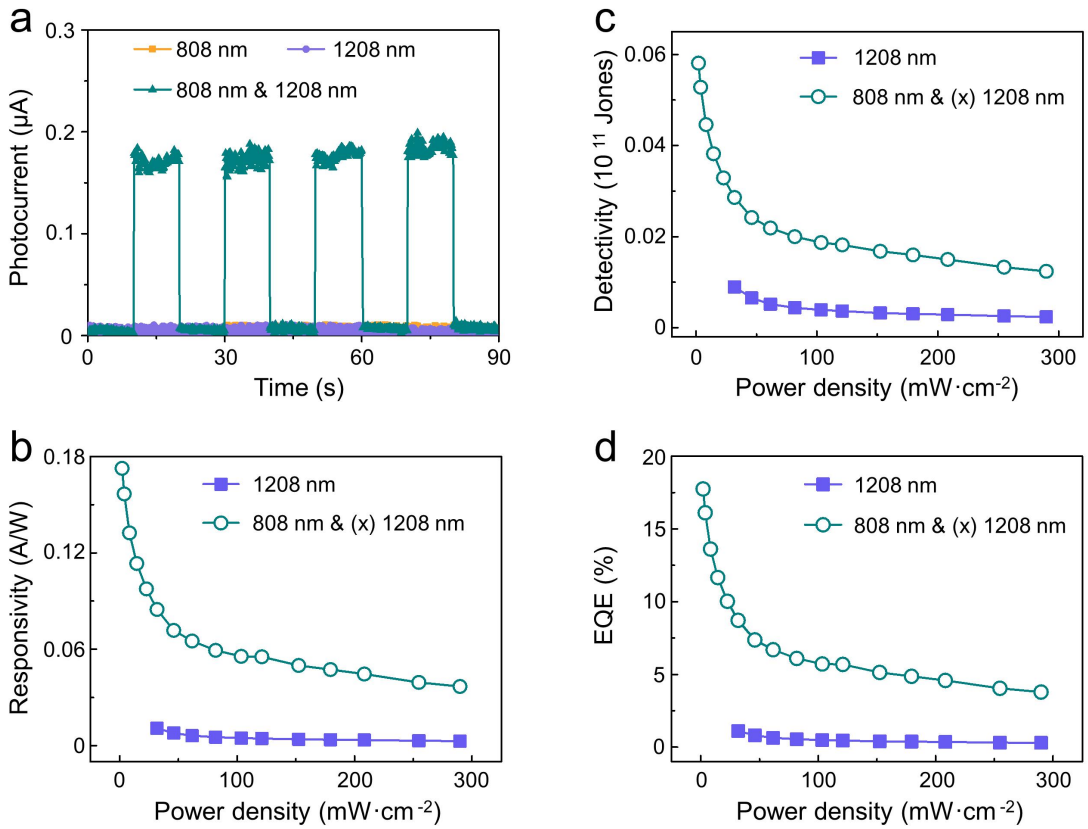

Supplementary Figure 28. The detection performance of $NaYS_2$:Ho^{3+},Yb^{3+}-based PDs. (a) On/off time-dependent photocurrent curves of photodetector under independent excitation of 1208 nm or 808 nm and cooperative excitation of 1208 nm and 808 nm in Ho^{3+}, Yb^{3+} based PDs. Power density dependence of (b) photoresponsivity (*R*), (c) detectivity and (d) external quantum efficiency (*EQE*) for 1208 nm NIR light detection with or without 808 nm light assistance.

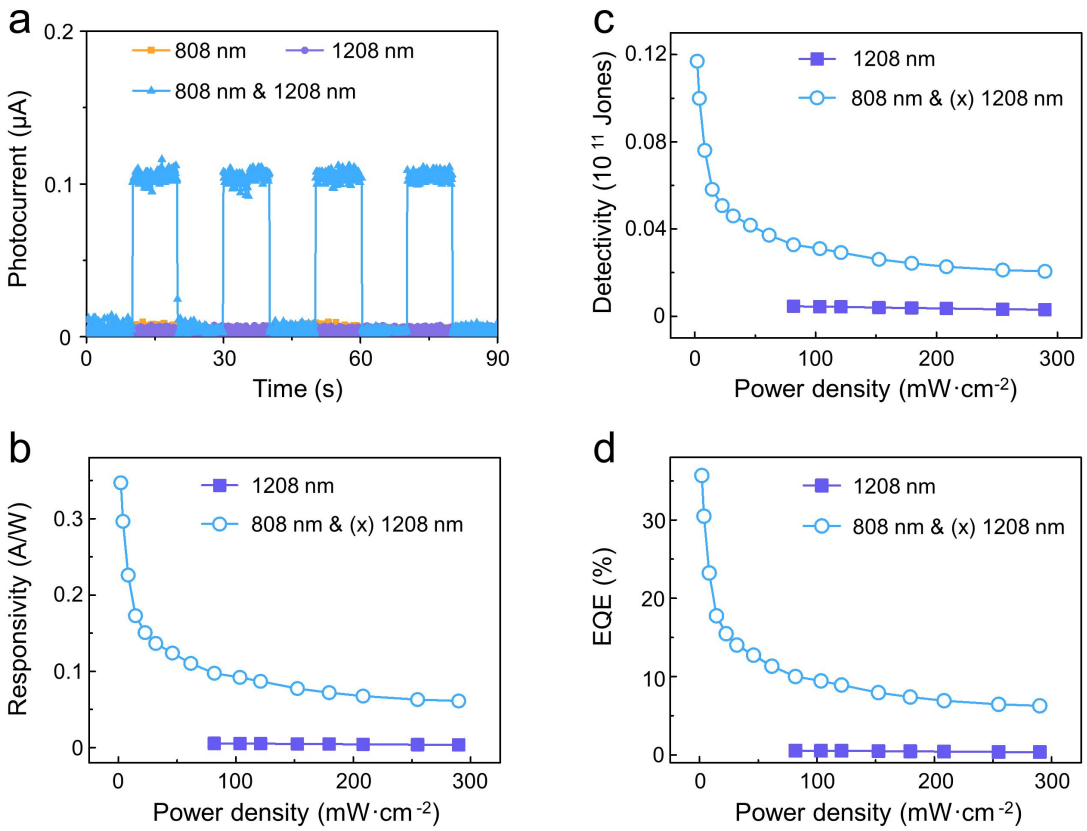

Supplementary Figure 29. The detection performance of $NaYS_2$:Ho^{3+},Tm^{3+}-based PDs. (a) On/off time-dependent photocurrent curves of photodetector under independent excitation of 1208 nm or 808 nm and cooperative excitation of 1208 nm and 808 nm in Ho^{3+}, Tm^{3+} based PDs. Power density dependence of (b) photoresponsivity (*R*), (c) detectivity and (d) external quantum efficiency (*EQE*) for 1208 nm NIR light detection with or without 808 nm light assistance.

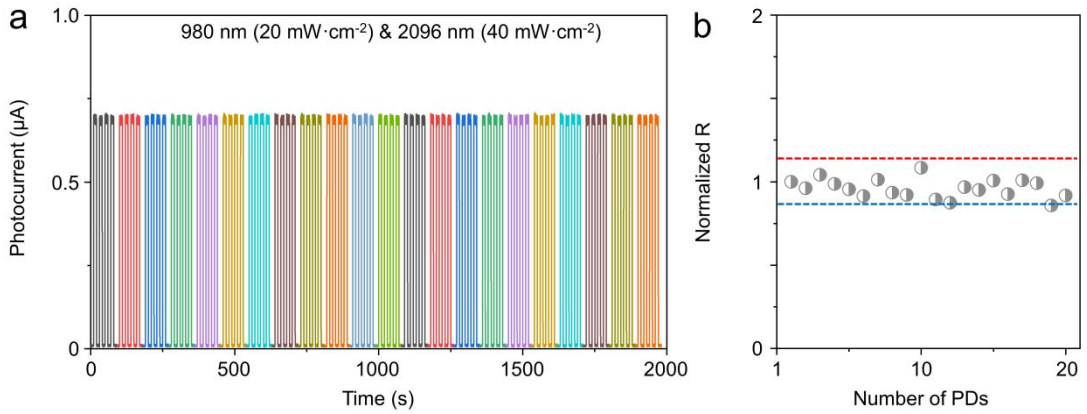

Supplementary Figure 30. Stability test of $NaYS_2:Ho^{3+}$-based PDs. (a) Cyclic on/off illumination tests using 980 nm (20 mW·cm^{-2}) and 2096 nm light (40 mW·cm^{-2}) over a 2000-second duration. The peak photocurrent amplitude remains nearly unchanged across all on/off cycles, with no observable decay in signal magnitude over 2000 s of continuous operation (b) The normalized *R* of the prepared 20 independent PDs under identical conditions. The normalized *R* of all devices falls within a narrow range of ±10% relative to the average value.

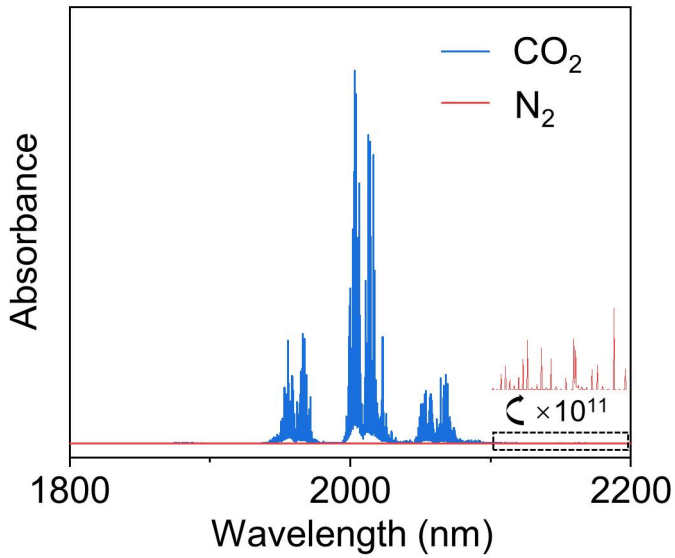

Supplementary Figure 31. Absorption of CO_2 and N_2 gas ranging from 1800 nm to 2200 nm. The strong absorption of CO_2 contrasts sharply with the extremely weak absorption of N_2, with a difference exceeding 11 orders of magnitude. N_2 causes virtually no interference in the characteristic absorption band of CO_2, enabling high-sensitivity quantitative detection of CO_2 concentration by monitoring the absorption peak near 2004 nm.

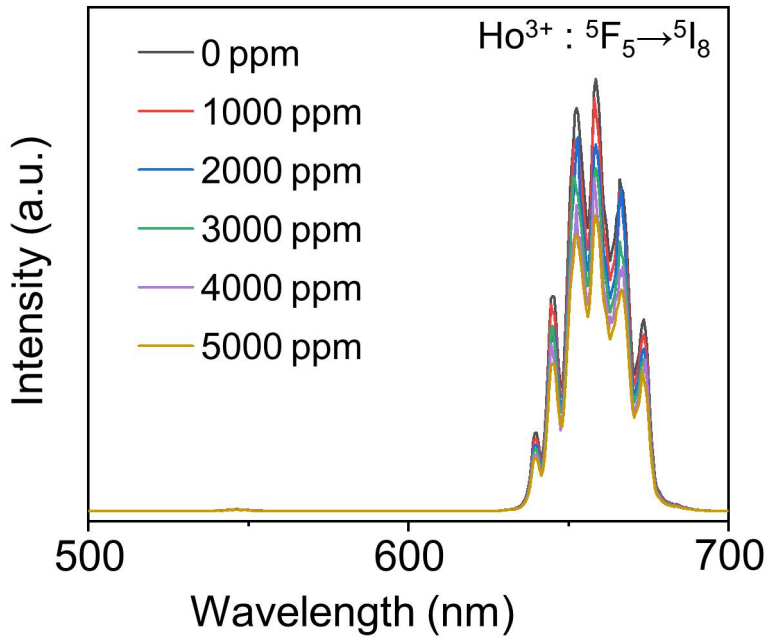

Supplementary Figure 32. CO_2 concentration-dependent UC emission properties. UC emission of fabricated PDs at different concentrations of CO_2 (0, 1000, 2000, 3000, 4000, 5000 ppm).

Supplementary References

[1] Fang, G. Q. Hasi, W. Lin, X. & Han, S. Automated identification of pesticide mixtures via machine learning analysis of TLC-SERS spectra, *J. Hazard. Mater.* **474**, 134814 (2024).

[2] Lin, S. et al. Ultrasensitive detection and distinction of pollutants based on SERS assisted by machine learning algorithms. *Sens. Actuat. B-Chem.* **384**, 133651 (2023).

[3] Xiao, M. & Selvin, P. R. Quantum yields of luminescent lanthanide chelates and far-red dyes measured by resonance energy transfer, *J. Am. Chem. Soc.* **123**, 7067-7073 (2001).

[4] Cao, B. S. et al. Wide-range and highly-sensitive optical thermometers based on the temperature-dependent energy transfer from Er to Nd in Er/Yb/Nd codoped $NaYF_4$ upconversion nanocrystals, *Chem. Eng. J.* **385**, 123906 (2020).